

**Advanced process-synchronized computed tomography for the investigation of periodic processes**

Bieberle, A.; Neumann, M.; Hampel, U.;

Originally published:

July 2018

**Review of Scientific Instruments 89(2018), 073111**

DOI: <https://doi.org/10.1063/1.5038423>

Perma-Link to Publication Repository of HZDR:

<https://www.hzdr.de/publications/Publ-27330>

Release of the secondary publication  
on the basis of the German Copyright Law § 38 Section 4.

1                   Advanced process-synchronized computed tomography  
2                   for the investigation of periodic processes

3                   André Bieberle<sup>1</sup>, Martin Neumann<sup>1,2</sup>, Uwe Hampel<sup>1,2</sup>

4                   <sup>1</sup> Institute of Fluid Dynamics, Helmholtz-Zentrum Dresden - Rossendorf,  
5                   Bautzner Landstr. 400, 01328 Dresden, Germany.

6                   <sup>2</sup> AREVA Endowed Chair of Imaging Techniques in Energy and Process Engineering,  
7                   Technische Universität Dresden, 01062 Dresden, Germany.

8                   Email: a.bieberle@hzdr.de

9  
10 **Abstract**

11                   Computed tomography (CT) is known for giving cross-sectional images of a body. As  
12                   tomographic scans require mechanical movement of components, data acquisition is  
13                   commonly too slow to capture dynamic processes, which are faster than the acquisition  
14                   time for a single image. Time-averaged angle-resolved CT imaging is a more recent  
15                   method, which has demonstrated a capability to sharply image fast rotating machinery  
16                   components by synchronizing data acquisition with rotation. However, in this modality  
17                   all information on static parts disappear. In this paper, a novel data acquisition approach  
18                   is introduced that combines both CT imaging methods. Eventually, the developed  
19                   method is exemplarily applied to the study of gas-liquid flow in an industrial centrifugal  
20                   pump using high-resolution gamma-ray tomography imaging.

21  
22 **Key words**

23                   Tomographic imaging, synchronized data acquisition, multiphase flow, centrifugal pump  
24

## 25 1 Introduction

26 Radiation based computed tomography (CT) is widely used for non-destructive testing, non-intrusive  
27 process analyses as well as for medical diagnostics. For conventional tomographic imaging,  
28 radiographic projections are acquired from different angular positions of the object of investigation  
29 by either rotating a source-detector assembly around the fixed object or by rotating the object in  
30 between the source and detector. Subsequently, the recorded attenuation projections are  
31 reconstructed to a cross-sectional image using e.g. filtered back projection or algebraic  
32 reconstruction techniques. The resulting images give the non-superimposed attenuation coefficient  
33 map of the object slice or volume [1]-[3].

34 Conventional radiographic computed tomography (*convCT*) was originally developed for medical  
35 diagnostics with X-rays. Here, the patient is placed between a mechanically rotating source-detector  
36 assembly that continuously acquires slice images with high spatial resolution [4]-[6]. By synchronizing  
37 the progressive feed of the patient through the CT scanner, so-called helical CT imaging is performed  
38 providing complete volume scans of the body [7]. Furthermore, such full body CT scans are  
39 meanwhile synchronized with the electrocardiogram signals from the heart's systolic and diastolic  
40 phases in order to avoid motion artefacts [8]-[10]. Such synchronized CT imaging is also referred to as  
41 process-synchronized computed tomography (*psCT*).

42 Meanwhile, computed tomography is an emerging technique for many industrial applications, too.  
43 Non-destructive testing is often applied for quality control of technical components and materials for  
44 example to detect inclusions, contact faults, fissures and cracks in integrated circuits, engines for  
45 aerospace applications but also for positioning and inspection of human implants [11]-[13]. Here,  
46 mainly X-ray tomography scanners have been developed and commercialized, providing images at  
47 high spatial resolution of static objects. In contrast, process tomography for troubleshooting,  
48 optimization and predictive maintenance in process equipment, such as chemical reactors, pumps or  
49 heat exchangers relies mainly on gamma radiation [14]-[19]. Harsh process environments, process  
50 dynamics, occurrence of multiphase flow as well as rotating equipment pose additional challenges  
51 for reliable CT imaging with respect to dynamic imaging. So far, process tomography has been  
52 applied mainly in a conventional manner providing time-averaged slice images of the material or  
53 fluid phase distributions, e.g. in various chemical reactors [20]-[27]. However, information about the  
54 process dynamics is often lost.

55 As a first step towards process-synchronized imaging, Prasser et al. (2003) introduced a novel CT  
56 imaging method called time-averaged angle-resolved CT (*tarCT*). They demonstrated the visualization  
57 of periodically changing gas fraction fields in an axial pump by synchronizing the data acquisition with  
58 the rotating parts of the pump and using an in-house developed radiation detector arc whose  
59 sampling frequency was significantly higher than the rotation frequency of the pump impeller [28].  
60 With this approach, multiphase flows within various rotating equipment, e.g. stirred tanks [29], axial  
61 pumps [28], centrifugal pumps [32]-[34] and couplings [30]-[31], were further successfully studied. It  
62 should be mentioned that such synchronized CT data acquisition and imaging is not limited to  
63 rotating parts but can also be triggered by any kind of regular process intermittency such as periodic  
64 pulsation or flashing conditions as present for Taylor flow in capillaries [35] or for fuel injection in  
65 plunger pumps [36].

66 Hitherto, either *convCT* or *tarCT* have been applied exclusively for multiphase flow investigations in  
67 rotating systems. Applying both CT imaging methods simultaneously would a) reduce the CT imaging  
68 time, b) improve the reliability and interpretability of static and dynamic results if the steady state of  
69 the process cannot be guaranteed and c) provide unique data on the dynamics of multiphase flows in  
70 process equipment with periodic behavior. The latter means, static as well as periodic parts can be  
71 reconstructed sharply. Eventually, images can be compiled as a sequence, which then shows the  
72 dynamics of a process along a period of the intermittency.

73 In the following, a novel approach for the simultaneous imaging with *convCT* and *tarCT* is introduced,  
74 which we refer to as advanced process-synchronized CT (*advCT*). The new method has been  
75 exemplarily applied to an industrial centrifugal pump operated in single-phase and two-phase flow  
76 conditions. As CT imaging system the high-resolution gamma-ray CT scanner [14], [29] was  
77 accordingly modified and applied.

78

## 79 2 Materials and Methods

### 80 2.1 CT imaging techniques

81 In general, computed tomography can be performed with either photon integrating detectors,  
82 delivering an analogue electrical voltage signal whose amplitude is proportional to the radiation  
83 photon flux, or photon counting detectors, delivering a digital number of radiation photons that are

84 counted within a projection interval. Since the CT system used in this study operates in photon  
 85 counting mode, *advCT* imaging is described in the following using the count rate notation.

86 *Computed tomography* bases on the acquisition of radiographic projections of an object from  
 87 different angular positions. For each projection  $i \in \mathbb{N} \mid 0 \leq i < N_\varphi$  the radiation intensity profile for  
 88 all detector elements  $d \in \mathbb{N} \mid 0 \leq d < N_d$  is stored in terms of counted radiation photons in a data  
 89 matrix  $S_{d,i}$ . Thus, the count rates

$$90 \quad \dot{S}_{d,i} = S_{d,i}/\Delta t_i \quad (1)$$

91 with the sampling interval  $\Delta t_i$  of each projection  $i$ . A reference CT scan  $\dot{S}_{d,i}^{\text{ref}}$  without object or with  
 92 the object in a reference state is used to calculate the radiation attenuation data matrix (sinogram)

$$93 \quad E_{d,i} = -\ln\left(\frac{\dot{S}_{d,i}}{\dot{S}_{d,i}^{\text{ref}}}\right). \quad (2)$$

94 These data are then used to reconstruct the non-superimposed slice image of the averaged  
 95 attenuation coefficients.

96 For *convCT imaging* the source-detector assembly (or respectively the object) is rotated with a slow  
 97 rotation frequency  $f^{\text{CT}}$  and provides  $N_\varphi$  radiographic projections during a full  $0^\circ \leq \varphi < 360^\circ$   
 98 rotation. Accordingly, the corresponding detector sampling frequency  $f^{\text{samp}}$  is defined by

$$99 \quad f^{\text{samp}} = N_\varphi \cdot f^{\text{CT}}. \quad (3)$$

100 This way, a data matrix  $\dot{S}_{d,i}^{\text{conv}}$  of dimension  $N_d \times N_\varphi$  is obtained wherein stationary parts of the  
 101 object appear as sinusoidal structures. Thus, applying any CT reconstruction algorithm to the  
 102 resulting  $E_{d,i}^{\text{conv}}$ , static parts such as housings, baffles and nozzles are sharply reconstructed while  
 103 moving parts, like rotating impellers, are smeared across the imaging plane (see Figure 1a).

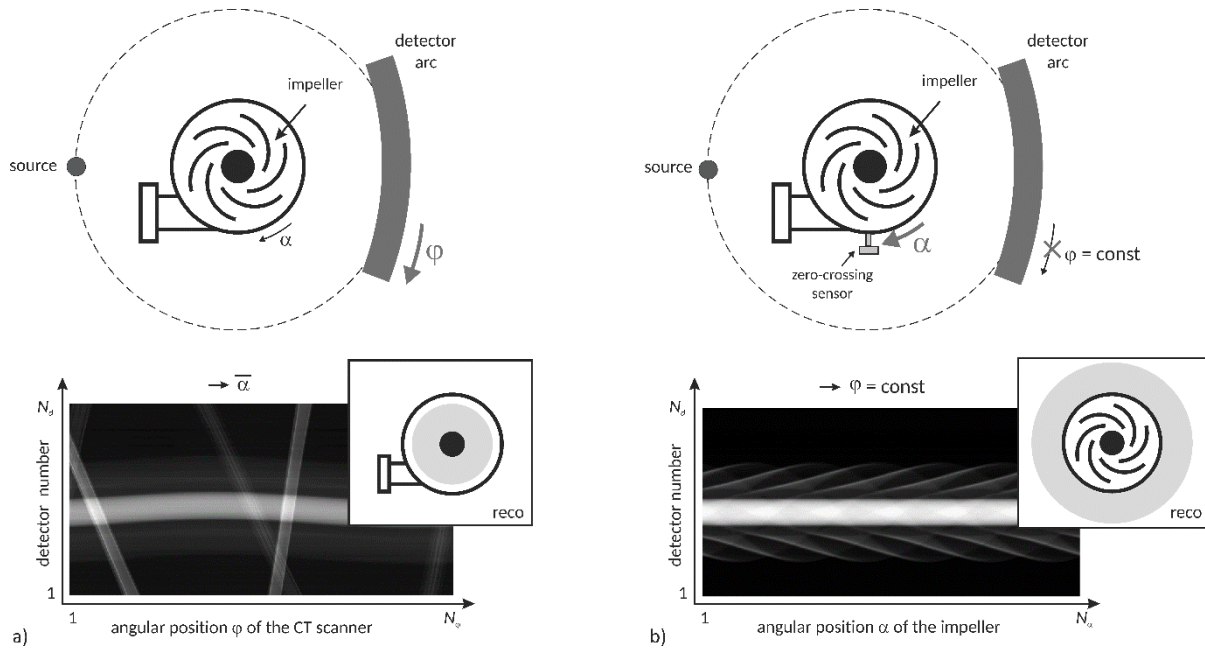
104 For *tarCT imaging*, the source-detector assembly is not rotated, i.e.  $f^{\text{CT}} = 0$ . Instead, the projection  
 105 data acquisition is synchronized with periodically moving (rotating) parts of the object. In case of an  
 106 impeller rotating with a given frequency  $f^{\text{rot}}$ , projection data are continuously sampled at a high  
 107 frequency  $f^{\text{samp}}$ . Accordingly, the number of projections is given by

$$108 \quad N_\alpha = f^{\text{samp}}/f^{\text{rot}}, \quad (4)$$

109 whereas  $f^{\text{samp}}$  must be significantly larger than  $f^{\text{rot}}$ . Typically, the statistics of detected photons  
 110 within a single projection, i.e. the number of incident radiation photons in each single detector

111 element, is too low. Hence, all values of each detector element of each projection angle are added  
 112 over a sufficient number of cycles, e.g. impeller revolutions. Synchronization can be performed by  
 113 recording the signal of any suitable revolution sensor simultaneously with the projection data. In  
 114 case of a rotating impeller, a Hall effect sensor might provide a zero-crossing signal for each  
 115 revolution that corresponds to an acquisition interval  $\Delta t_{zc} = 1/f^{\text{rot}}$ . Then, each detector reading  
 116 (projection with index  $j \in \mathbb{N} \mid 0 \leq j < N_\alpha$ ) corresponds to one angular position  $\alpha_j = 2\pi j/N_\alpha$  of the  
 117 impeller. Hence, the dimension of the data matrix  $\hat{S}_{d,j}^{\text{tar}}$  is  $N_d \times N_\alpha$ .

118



119

120 **Figure 1:** Scheme of setup and imaging procedure (top), obtained sinograms (bottom) and schematic view of  
 121 reconstructed images (inset) with sharp (black) and angular-averaged (gray) structures exemplarily shown for a  
 122 centrifugal pump applying a) *convCT* and b) *tarCT* imaging.

123 As mentioned above, for *tarCT* imaging projection data have to be acquired for a number of rotations  
 124  $N_r$ . Thus, a three-dimensional data matrix  $S_{d,j,t}^{\text{tar}}$  is initially generated, where the index  $t$  is defined as  
 125  $t \in \mathbb{N} \mid 0 \leq t < N_r$  and the index  $j$  is defined as  $j = N_\alpha \Delta t_j / \Delta t_{zc}$ . The interval  $\Delta t_j$  denotes the  
 126 residual time since the last zero-crossing. By integrating over all revolutions and dividing by the total  
 127 time  $t_{zc} \cdot N_r / N_\alpha$  per projection angle, the count rates

128

$$\hat{S}_{d,j}^{\text{tar}} = \frac{1}{t_{zc} \cdot N_r / N_\alpha} \cdot \sum_{t=1}^{N_r} S_{d,j,t}^{\text{tar}} \quad (5)$$

129

129 are calculated representing radiographic projections of the rotating parts of the pump taken in the  
 130 rotating frame, i.e. the impeller and all the parts including the liquid holdup rotating at the same  
 131 speed (see Figure 1b).

132 For *advCT imaging* both previously described CT imaging methods are simultaneously performed. To  
 133 obtain the sinogram data for *convCT* and *tarCT* from one measurement, a three-dimensional data  
 134 matrix  $\dot{S}_{d,i,j}^{\text{adv}}$  of the dimensions  $N_d \times N_\varphi \times N_\alpha$  is defined at first (see Figure 2, middle). The source-  
 135 detector assembly is then rotated around the object. At the first quasi-stationary projection position  
 136  $i = 1, \varphi_0 = 0^\circ$  a time-averaged angle-resolved data set  $\dot{S}_{d,i=1,j}^{\text{adv}} = \dot{S}_{d,j}^{\text{tar}}$  is obtained according to the  
 137 procedure described above. This is repeated for each subsequent projection angle  $\varphi_i =$   
 138  $2\pi(i-1)/N_\varphi$ . After an entire rotation of the source-detector assembly  $\dot{S}_{d,i,j}^{\text{adv}}$  contains  $N_\varphi$  sub-  
 139 matrices with  $i \in \mathbb{N} \mid 0 \leq i < N_\varphi$  each representing a single time-averaged angle-resolved sinogram  
 140 obtained by varying the projection angle  $\varphi_i = 2\pi i/N_\varphi$  of the source-detector assembly (see Figure  
 141 2, top).

142 Given the object to be positioned in the very center of the source-detector assembly and provided  
 143 that  $N_\varphi = N_\alpha$ , an extended time-averaged angle-resolved sinogram

$$144 \quad \dot{S}_{d,j}^{\text{tar}} = \frac{1}{N_\varphi} \cdot \sum_{i=1}^{N_\varphi} \dot{S}_{d,i,j^*}^{\text{adv}} \quad \text{with } j^* = (j - i) \bmod j \quad (6)$$

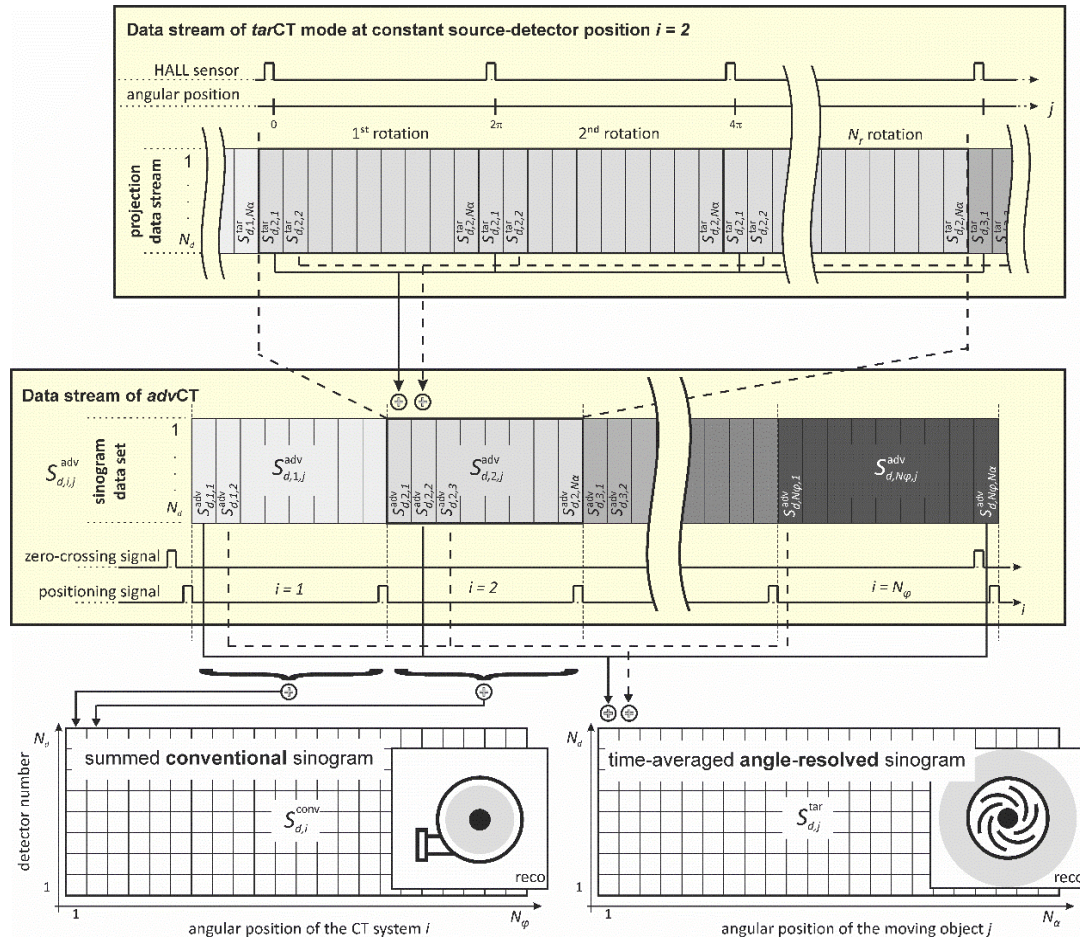
145 can simply be obtained by averaging shifted versions of  $\dot{S}_{d,i,j}^{\text{adv}}$  containing projections with the best  
 146 photon statistic. The projection shift  $j^* = (j - i) \bmod j$  in  $\dot{S}_{d,i,j^*}^{\text{adv}}$  compensates the angular offset  
 147 between the applied *tarCT* synchronization sensor, e.g. Hall sensor, and the associated projection  
 148 angle  $\varphi_i$  of the CT imaging system (see Figure 2, bottom, right). Averaging  $\dot{S}_{d,i,j}^{\text{adv}}$  over all rotation  
 149 angles  $j$ , the conventional sinogram

$$150 \quad \dot{S}_{d,i}^{\text{conv}} = \frac{1}{N_\alpha} \cdot \sum_{j=1}^{N_\alpha} \dot{S}_{d,i,j}^{\text{adv}} \quad (7)$$

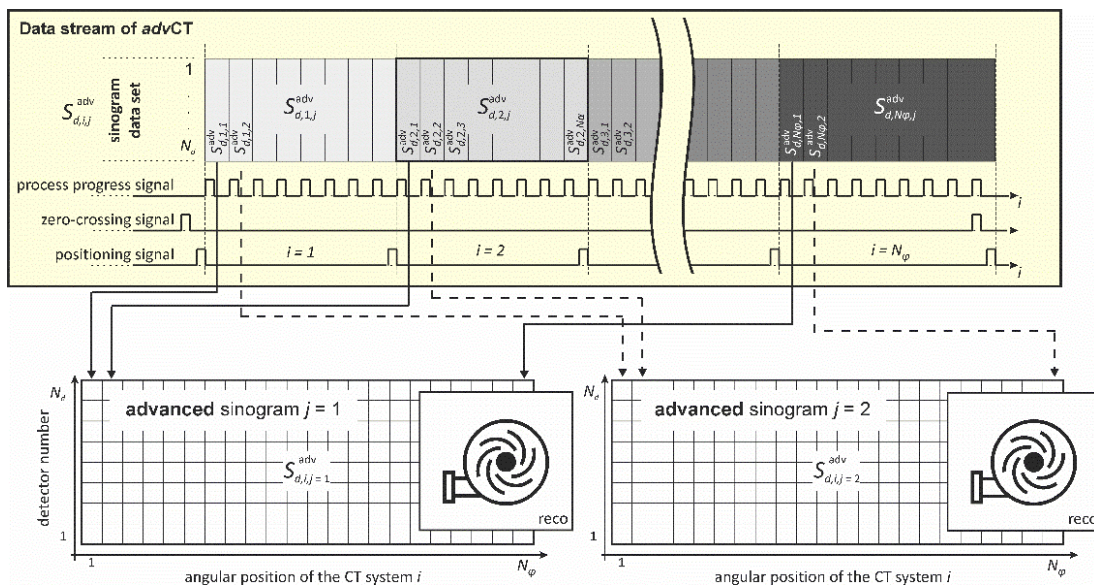
151 is obtained (see Figure 2, bottom, left).

152 For each  $j$  the sub-matrix  $\dot{S}_{d,i,j=\text{const}}^{\text{adv}}$  represents a conventional sinogram for a given (static) impeller  
 153 angle position (see Figure 3). Eventually, a combined image can be reconstructed showing both the  
 154 focused stationary structures as well as the rotating structures ‘frozen’ at an angular position  $\alpha_j =$   
 155  $2\pi j/N_\alpha$ . It should be mentioned, that the image is still an ensemble-average obtained over many  
 156 rotations. Nevertheless, this combined CT imaging approach is practical, if structures in the object  
 157 change repeatedly with the identical course for every revolution. In case of the centrifugal pump, this  
 158 holds for fluid elements that enter the pump in the center and move towards the tangential outlet.  
 159 Thus, such permanently occurring radial flow can be visualized with this CT imaging mode. Therefore,

160 frozen-impeller images are reconstructed for all impeller angles  $\alpha$ . The resulting image sequence  
 161 shows how ensemble-averaged structures move with the rotating impeller during one revolution.



162  
 163 **Figure 2:** Schematics of the projection data stream analysis to restructure projection data according to both *tarCT* and  
 164 *convCT* using a data set provided by the *advCT* imaging method.



165  
 166 **Figure 3:** Schematics of the projection data stream analysis to restructure projections according to *advCT* for two different  
 167 angular positions of the impeller, which rotates at 1480 rpm.

## 168 2.2 Gamma-ray CT scanner

169 The applied high-resolution gamma-ray CT scanner (HireCT) mainly comprises a collimated  $^{137}\text{Cs}$   
170 source with an activity of about 185 GBq and a photon energy of 662 keV as well as a radiation  
171 detector arc composed of  $N_d = 320$  scintillation detector elements positioned opposite to the  
172 source. Each detector pixel has an active area of 2 mm by 4 mm and provides a radiation detection  
173 efficiency of about 75% for 662 keV gamma photons. The detector arc is focused to a distance of  
174 970 mm and is operated in single photon count mode, which is very important at low photon fluxes,  
175 high projection data sampling frequencies or at a combination of both. Hitherto, the HireCT was  
176 operated in either *convCT* or *tarCT* imaging mode [14], [29].

177 For *convCT* imaging, the HireCT is typically rotated slowly between  $f^{\text{CT}} = 0.33$  mHz (0.02 rpm) and  
178  $f^{\text{CT}} = 1.67$  mHz (0.1 rpm). Accordingly, the data sampling frequency and its corresponding data  
179 stream rate is rather low and hence not critical. The projection data acquisition is triggered by two  
180 light barrier sensors directly mounted on the rotary stage. The first light barrier indicates the zero-  
181 crossings, i.e. angular reference position. The second sensor delivers a crossing signal at every  $0.36^\circ$   
182 interval using a mechanically perforated ring with  $N_\phi = 1000$  equidistantly distributed measuring  
183 points.

184 For *tarCT* imaging, the HireCT is fixed and provides a projection data sampling frequency of up to  
185  $f^{\text{samp}} = 22$  kHz, which is sufficient to sample rapidly moving parts, such as impellers of axial and  
186 centrifugal pumps [33] or fluid couplings [30], [31]. Therefore, an additional very fast data acquisition  
187 and transfer electronics is used and an advanced detector value read-out procedure is performed.  
188 For process-synchronization, two binary status signals are connected to the electronics and are  
189 directly implemented into the projection data stream.

190 To perform *advCT* imaging, the positioning information of the HireCT is recorded with the existing  
191 fast data acquisition and transfer electronics. Therefore, the electrical signals of both light barrier  
192 sensors were initially connected to the existing microprocessor via a dual optoelectronic coupler.  
193 Further, the microprocessor firmware was modified to integrate the binary status of both light  
194 barrier sensors into the existing status byte, in which already two status signals for the process  
195 synchronisation sensors were coded. This way, the modified fast data acquisition electronics is able  
196 to sample four external binary signals, while the size of the data stream and the data sampling  
197 frequency  $f^{\text{samp}}$  is retained.

### 198 3. Results

199 The *advCT* imaging mode and the modified HireCT scanner are applied to an industrial centrifugal  
200 pump (Etachrom BC 032-160074 C11, KSB, Germany) with a closed radial multi-vane impeller forming  
201 six fluid conveying chambers. The pump was already investigated by Schäfer et al. [34] and Neumann  
202 et al. [33] concerning their gas-liquid flow operation behaviour. In this study, a constant volumetric  
203 gas fraction of 2.6 % is charged with the conveyed liquid (tap water). The diameter of the impeller is  
204 125 mm, which rotates with a speed of  $f^{\text{pump}} = 1480$  rpm. An external Hall effect sensor provides  
205 the zero-crossing signals for each revolution of the pump impeller corresponding to a time interval of  
206  $\Delta t_{zc} = 40.54$  ms per revolution.

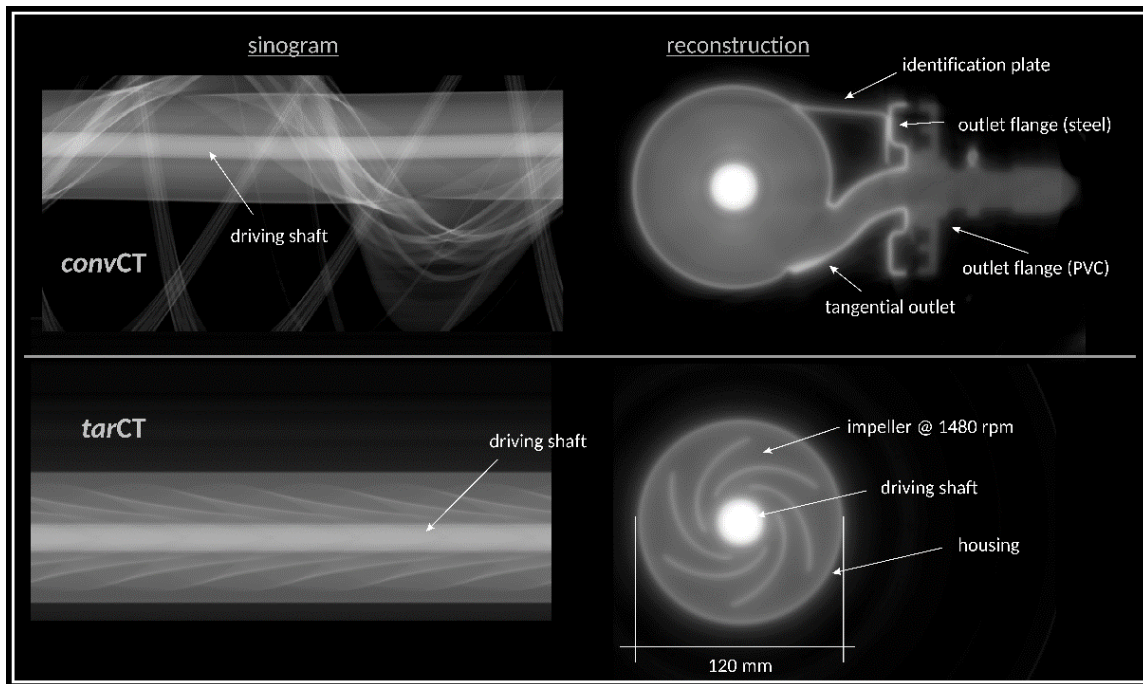
207 Eventually, *advCT* of the centrifugal pump operated with single-phase liquid and two-phase  
208 gas/liquid flow are performed with a total duration of 50 min, i.e. each *tarCT* scan is performed for  
209 three seconds. A single projection scan  $\hat{S}_d^{\text{ref}}$  without any object and with sufficient photon statistic is  
210 used as reference for calculating the absolute radiation attenuation values. Projection data pre- and  
211 post-processing are accomplished as described in Chapter 2.2 using GNU Octave v4.2.1.  
212 Simultaneous iterative reconstruction technique (SIRT) was performed with 50 iteration steps on a  
213 graphic processing unit by the open-source CT reconstruction tool ASTRA v1.8 [37]-[39]. Slice images  
214 are reconstructed on a  $1440 \times 1440$  pixel grid with a pixel size of 0.5 mm. For this purpose, the  
215 obtained fan beam sinogram is resorted and interpolated to a parallel beam sinogram with virtual  
216 3600 detector elements and 1800 projections for a  $180^\circ$  rotation.

217 As shown in Figure 4, the results of both standard CT imaging methods (*convCT* and *tarCT*) could be  
218 successfully extracted from the *advCT* scan using Equations (6) and (7). It can be seen from the  
219 *convCT* sinogram that the driving shaft of the impeller is not exactly positioned in the very centre of  
220 the HireCT system. Thus, in addition to Equation (6), each *tarCT* sinogram  $\hat{S}_{d,t=\text{const},j}^{\text{adv}}$  is slightly  
221 shifted along the detector axis to achieve an overlap of the driving shaft in the final averaged *tarCT*  
222 sinogram  $\hat{S}_{d,j}^{\text{tar}}$ . The empirically identified shifting sinus curve from the *convCT* will reduce the optimal  
223 spatial resolution of the *tarCT* scan to a negligible degree.

224 Prior to reconstructing the image sequence from the *advCT*, the following additional artificial process  
225 synchronisation is performed. As the impeller consists of six identical constructed and rotation-  
226 symmetrically arranged chambers, each sixth part of the sinogram  $\hat{S}_{d,i,j}^{\text{adv}}$  is averaged with respect to  $j$   
227 (see Figure 5) in order to significantly improve the photon statistic. Nevertheless, possible pulsations

228 of the gas phase towards the tangential outlet of the centrifugal pump are still visible in the averaged  
 229 *adv*CT sinogram stack  $\dot{S}_{d,i,j}^{\text{adv}}$  with  $N_\alpha = N_\alpha/6$ . In Figure 6, five exemplarily reconstructed cross-  
 230 sectional images are shown in which the impeller is visualised in different angular positions ranging  
 231 from  $0^\circ$  to  $48^\circ$  with increments of  $12^\circ$  (note that the  $60^\circ$  position coincides with the  $0^\circ$  position).

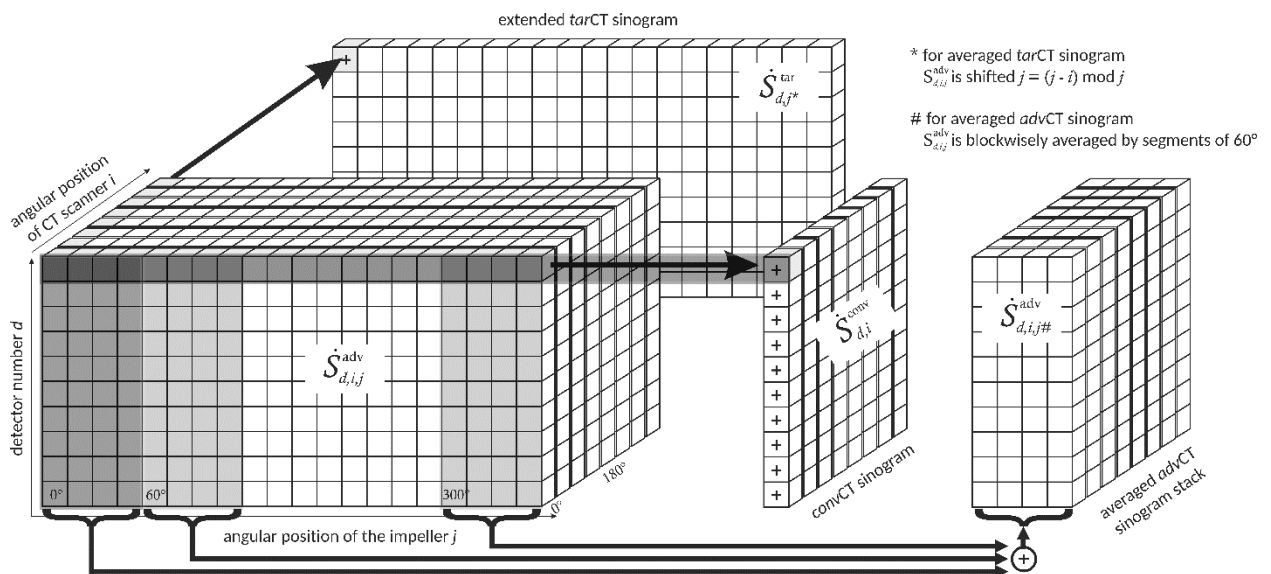
232



233

234 **Figure 4:** Comparison of *conv*CT imaging (top) and *tar*CT imaging (bottom) using the improved electronics of the HireCT for  
 235 the centrifugal pump (impeller is rotating with 1480 rpm) that enables *adv*CT imaging.

236

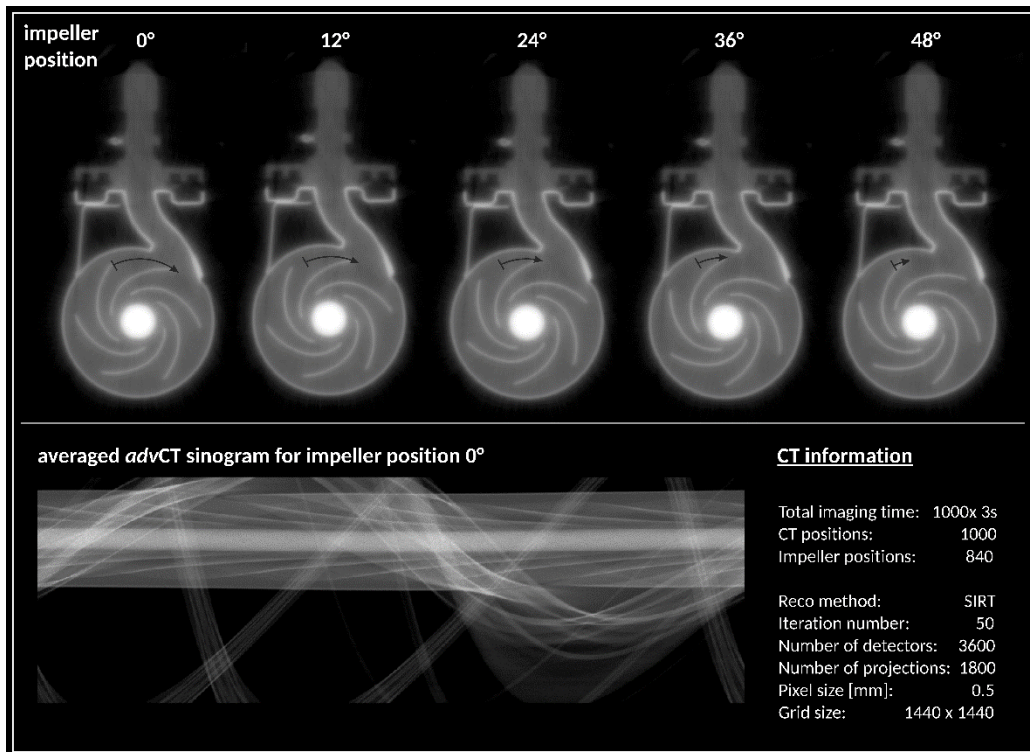


237

238 **Figure 5:** Illustration of the data sorting procedure of the *adv*CT data stack to extract *conv*CT and *tar*CT sinograms and an  
 239 averaged *adv*CT sinogram stack as well.

240 For the calculation of the gas fraction distributions, reconstructed absolute images of the centrifugal  
241 pump operated at two-phase flow conditions are subtracted with the images obtained from the  
242 centrifugal pump operated at single-phase liquid flow conditions and subsequently normed to the  
243 attenuation value of the liquid phase. The results are compiled in Figure 7. For a better orientation,  
244 an absolute reconstruction of the centrifugal pump is shown in the top left position.

245



246

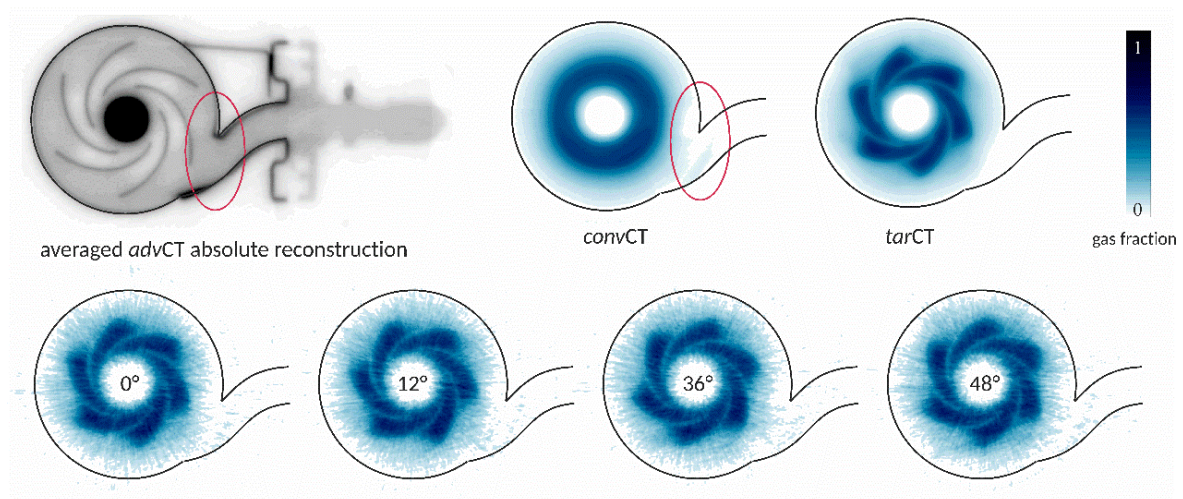
247 **Figure 6:** Reconstructions of the centrifugal pump at five different angular positions of its impeller operated at 1480 rpm.

248

249 From the averaged *convCT* imaging (Figure 7, top, centre) an asymmetric gas pocket is identified near  
250 the tangential outlet of the centrifugal pump (highlighted by the red circle), representing  
251 continuously ejected gas fraction. Furthermore, *convCT* imaging reveals a gas dead zone directly  
252 behind the tangential outlet. In contrast, the result from averaged *tarCT* imaging (Figure 7, top, right)  
253 shows no asymmetric gas phase distribution with respect to the impeller geometry. However, it can  
254 be recognized that the gas phase is homogeneously distributed in all six chambers and the gas  
255 fraction is significantly higher compared to the injected volumetric gas fraction of 2.6 %. Thus, it can  
256 be concluded that a static or dynamic gas pocket is generated within the impeller region that  
257 impedes the transport of the liquid (see also [33], [34]).

258 Eventually, the image sequence obtained by the averaged *advCT* imaging procedure is visualized for  
259 selected angular positions of the impeller (Figure 7, bottom). Again gas-rich and gas-lean zones can  
260 be identified. In contrast to the averaged *tarCT*, both scenarios can now be studied in its dynamics,  
261 i.e. depending on the angular position of the impeller.

262



263

264 **Figure 7:** Visualization of the gas fraction distribution in a centrifugal pump (top, left) operated in gas-liquid two-phase flow  
265 applying *advCT* imaging using the HireCT imaging system. Results of the *convCT* (top, centre), the *tarCT* (top, right)  
266 and results of the averaged *advCT* (bottom line) are shown. (Colours available in the online version)

267

## 268 4. Conclusion

269 In this paper, an advanced process-synchronized computed tomography (*advCT*) imaging approach  
270 was presented that combines the pros of two standard CT imaging methods, namely conventional CT  
271 (*convCT*) and time-averaged angle-resolved CT (*tarCT*). After presenting their basic principles, the  
272 *advCT* imaging was introduced from which data of both standard CT imaging methods can be  
273 extracted. Additionally, using a new data sorting procedure, cross-sectional image sequences at  
274 different process progress stages with sharp structures of both the static and the synchronized  
275 dynamic parts were obtained. The novel *advCT* was exemplarily proved on a centrifugal pump whose  
276 impeller rotated with 1480 rpm. Eventually, quantitative phase fraction distributions were calculated  
277 and investigated. Various static and dynamic flow processes could be clearly revealed. Thus, the  
278 amount of information was significantly increased using the novel *advCT* imaging.

279

## 280 5. References

- 281 [1] C. Kak, M. Slaney, Principles of Computerized Tomographic Imaging, *IEEE Press*, New York,  
282 (1988).
- 283 [2] R. Gordon, R. Bender, G. T. HERMAN, Algebraic Reconstruction Techniques (ART) for three-  
284 dimensional Electron Microscopy and X-ray Photography, *J. Theor. Biol.* 29, 471-481, (1970).
- 285 [3] Willi A. Kalender, Computed Tomography: Fundamentals, System Technology, Image Quality,  
286 Applications, 3rd Edition (2011), ISBN: 978-3-895-78317-3
- 287 [4] Wang Y, Vidan E, Bergman GW. Cardiac motion of coronary arteries: variability in the rest period  
288 and implications for coronary MR angiography. *Radiology* 213, 751-758, (1999).
- 289 [5] Flohr T, Kuttner A, Bruder H, et al. Performance evaluation of a multi-slice CT system with 16-  
290 slice detector and increased gantry rotation speed for isotropic submillimeter imaging of the  
291 heart. *Herz* 28, 7-19, (2003).
- 292 [6] Flohr T, Stierstorfer K, Raupach R, Ulzheimer S, Bruder H. Performance evaluation of a 64-slice  
293 CT system with z-flying focal spot. *Rofo* 176, 1803-1810, (2004).
- 294 [7] W.A. Kalender, W. Seissler, E. Klotz, P. Vock. Spiral volumetric CT with single-breathhold  
295 technique, continuous transport, and continuous scanner rotation. *Radiology*, 176/1, 181-183,  
296 (1990).
- 297 [8] M. Kachelrieß, S. Ulzheimer, W.A. Kalender. ECG-correlated imaging of the heart with subsecond  
298 multi-slice spiral CT. *IEEE Transactions on Medical Imaging* 19/9, 888-901, (2000).
- 299 [9] H. Seifarth, S. Wienbeck, M. Püsken, K.-U. Juergens, D. Maintz, Ch. Vahlhaus, W. Heindel, R.  
300 Fischbach, Optimal Systolic and Diastolic Reconstruction Windows for Coronary CT Angiography  
301 Using Dual-Source CT, *American Journal of Roentgenology* 189, 1317-1323, (2007).  
302 <https://doi.org/10.2214/AJR.07.2711>
- 303 [10] B. Lu, S.S. Mao, N. Zhuang, H. Bakhsheshi, H. Yamamoto, J. Takasu, S. Liu, M. J. Budoff, Coronary  
304 Artery Motion During the Cardiac Cycle and Optimal ECG Triggering for Coronary Artery Imaging,  
305 *Investigative Radiology* 36/5, 250-256, (2001).
- 306 [11] O. Lindgren, J. Davis, P. Wells, P. Shadbolt, Non-destructive wood density distribution  
307 measurements using computed tomography, *Holz als Roh-und Werkstoff* 50, 295, (1992).  
308 <https://doi.org/10.1007/BF02615356>

- 309 [12] I. Amenabar, A. Mendikute, A. López-Arraiza, M. Lizaranzu, J. Aurrekoetxea, Comparison and  
310 analysis of non-destructive testing techniques suitable for delamination inspection in wind  
311 turbine blades, *Composites Part B: Engineering* 42/5, 1298-1305, (2011).  
312 <https://doi.org/10.1016/j.compositesb.2011.01.025>
- 313 [13] D. J. Bull, L. Helfen, I. Sinclair, S. M. Spearing, T. Baumbach, A comparison of multi-scale 3D X-ray  
314 tomographic inspection techniques for assessing carbon fibre composite impact damage,  
315 *Composites Science and Technology* 75, 55-61, (2013).  
316 <https://doi.org/10.1016/j.compscitech.2012.12.006>
- 317 [14] U. Hampel, A. Bieberle, D. Hoppe, J. Kronenberg, E. Schleicher, T. Suehnel, W. Zimmermann,  
318 C. Zippe, High resolution gamma ray tomography scanner for flow measurement and non-  
319 destructive testing applications, *Review of Scientific Instruments* 78, 103704, (2007).
- 320 [15] A. Kemoun, B. C. Ong, P. Gupta, M. Al-Dahhan, M. P. Dudukovic, Gas holdup in bubble columns  
321 at elevated pressure via computed tomography, *International Journal of Multiphase Flow* 27,  
322 929-946, (2007).
- 323 [16] U.P. Veera, Gamma ray tomography design for the measurement of hold-up profiles in two-  
324 phase bubble columns, *Chemical Engineering Journal* 81, 251-260, (2001).
- 325 [17] A. Bieberle, H. Nehring, R. Berger, M. Arlit, H.-U. Härting, M. Schubert, U. Hampel, Compact  
326 high-resolution gamma-ray computed tomography system for multiphase flow studies, *Rev. Sci.*  
327 *Instrum.* 84, 033106, (2013).
- 328 [18] G. A. Johansen, T Frøystein, B. T. Hjertaker, Ø Olsen, A dual sensor flow imaging tomographic  
329 system, *Meas. Sci. Technol.* 7, 297-307, (1996).
- 330 [19] Kok, H.V., Hagen, T.H.J.J., Mudde, R.F., Subchannel void-fraction measurements in a 6×6 rod  
331 bundle using a simple gamma-transmission method, *International Journal of Multiphase Flow*  
332 27, 147-170, (2001).
- 333 [20] R. Rollbusch et al., Experimental investigation of the influence of column scale, gas density and  
334 liquid properties on gas holdup in bubble columns, *International Journal of Multiphase Flow* 75,  
335 88-106, (2015).  
336 <https://doi.org/10.1016/j.ijmultiphaseflow.2015.05.009>
- 337 [21] A. Bieberle et al., Gamma-ray computed tomography for imaging of multiphase flows, *Chemie*  
338 *Ingenieur Technik* Vol. 85 / 7, 1002-1011, (2013).  
339 <https://doi.org/10.1002/cite.201200250>

- 340 [22] H.-U. Haerting et al., Hydrodynamics of co-current two-phase flow in an inclined rotating tubular  
341 fixed bed reactor – Wetting intermittency via periodic catalyst immersion, *Chemical Engineering*  
342 *Science* 128, 147-158, (2015).  
343 <https://doi.org/10.1016/j.ces.2015.02.008>
- 344 [23] M. A. Leon et al., Hydrodynamics and Gas-Liquid Mass Transfer in a Horizontal Rotating Foam  
345 Stirrer Reactor, *Chemical Engineering Journal* 217/1, 10-21, (2012).  
346 <https://doi.org/10.1016/j.ces.2012.11.104>
- 347 [24] R. Tschentscher et al., Gas holdup of rotating foam reactors measured by  $\gamma$ -tomography - effect  
348 of solid foam pore size and liquid viscosity, *AIChE Journal* 59(1), 146-154, (2013).  
349 <https://doi.org/10.1002/aic.13787>
- 350 [25] R. Tschentscher et al., Tomography measurements of gas-holdup in rotating foam reactors with  
351 Newtonian, non-Newtonian and foaming liquids, *Chemical Engineering Science*, 66/14, 3317-  
352 3327, (2011).  
353 <https://doi.org/10.1016/j.ces.2011.01.051>
- 354 [26] M. Schubert, G. Hessel, C. Zippe, R. Lange, U. Hampel, Liquid flow texture analysis in trickle bed  
355 reactors using high-resolution gamma ray tomography, *Chemical Engineering Journal* 140/(1-3),  
356 332-340, (2008).
- 357 [27] F. Vischer et al., Water and n-heptane volume fractions in a rotor-stator spinning disc reactor,  
358 *Industrial & Engineering Chemistry Research* 51, 16670-16676, (2012).  
359 <https://doi.org/10.1021/ie301439s>
- 360 [28] H.-M. Prasser, D. Baldauf, J. Fietz, U. Hampel, D. Hoppe, C. Zippe, J. Zschau, M. Christen, G. Will,  
361 Time resolving gamma-tomography for periodically changing gas fraction fields and its  
362 application to an axial pump, *Flow Measurement and Instrumentation* 14, 119-125, (2003).
- 363 [29] A. Bieberle, E. Schleicher, U. Hampel, Data acquisition system for angle synchronized gamma-ray  
364 tomography of rapidly rotating objects, *Measurement Science and Technology* 18, 3384-339,  
365 (2007).
- 366 [30] U. Hampel, D. Hoppe, K.-H. Diele, J. Fietz, H. Höller, R. Kernchen, H.-M. Prasser, C. Zippe,  
367 Application of gamma tomography to the measurement of fluid distributions in a hydrodynamic  
368 coupling, *Flow Measurement and Instrumentation* 16, 85-90, (2005).
- 369 [31] A. Bieberle et al., Hydrodynamics analysis in micro-channels of a viscous coupling using gamma-  
370 ray computed tomography, *Flow Measurement and Instrumentation* 45, 288-297, (2015).  
371 <https://doi.org/10.1016/j.flowmeasinst.2015.07.008>

- 372 [32] H.-M. Prasser et al., Time Resolving Gamma-Tomography for Periodically Changing Gas Fraction  
373 Fields, *Flow Measurement and Instrumentation* 14, 119-125, (2003).  
374 [https://doi.org/10.1016/S0955-5986\(03\)00010-4](https://doi.org/10.1016/S0955-5986(03)00010-4)
- 375 [33] M. Neumann et al., An experimental study on the gas entrainment in horizontally and vertically  
376 installed centrifugal pumps, *Journal of Fluids Engineering* 138 (09130), 1-9, (2016).  
377 <https://doi.org/10.1115/1.4033029>
- 378 [34] T. Schaefer et al., Application of gamma-ray computed tomography for the analysis of gas  
379 holdup distributions in centrifugal pumps, *Flow Measurement and Instrumentation* 46, 262-267,  
380 (2015).  
381 <https://doi.org/10.1016/j.flowmeasinst.2015.06.001>
- 382 [35] M. Haghnegahdar, S. Boden, U. Hampel, Investigation of mass transfer in milli-channels using  
383 high-resolution microfocus X-ray imaging, *International Journal of Heat and Mass Transfer* 93,  
384 653-664, (2016).  
385 <https://doi.org/10.1016/j.ijheatmasstransfer.2015.10.033>
- 386 [36] A. Landelle, N. Tauveron, R. Revellin, P. Haberschill, S. Colasson, V. Roussel, Performance  
387 investigation of reciprocating pump running with organic fluid for organic Rankine cycle, *Applied*  
388 *Thermal Engineering* 113, 962-969, (2017).  
389 <http://dx.doi.org/10.1016/j.applthermaleng.2016.11.096>
- 390 [37] W. van Aarle, W. J. Palenstijn, J. Cant, E. Janssens, F. Bleichrodt, A. Dabravolski, J. De  
391 Beenhouwer, K. J. Batenburg, and J. Sijbers, "Fast and Flexible X-ray Tomography Using the  
392 ASTRA Toolbox", *Optics Express*, 24(22), 25129-25147, (2016).  
393 <http://dx.doi.org/10.1364/OE.24.025129>
- 394 [38] W. van Aarle, W. J. Palenstijn, J. De Beenhouwer, T. Altantzis, S. Bals, K. J. Batenburg, and J.  
395 Sijbers, "The ASTRA Toolbox: A platform for advanced algorithm development in electron  
396 tomography", *Ultramicroscopy*, 157, 35-47, (2015).  
397 <http://dx.doi.org/10.1016/j.ultramic.2015.05.002>
- 398 [39] W. J. Palenstijn, K. J. Batenburg, and J. Sijbers, "Performance improvements for iterative  
399 electron tomography reconstruction using graphics processing units (GPUs)", *Journal of*  
400 *Structural Biology*, vol. 176/2, 250-253, (2011).  
401 <http://dx.doi.org/10.1016/j.jsb.2011.07.017>